Journal of The Electrochemical Society, **156** (12) H961-H970 (2009)
0013-4651/2009/156(12)/H961/10/$25.00 © The Electrochemical Society

Nanoscale Defect Generation in CMP of Low-*k*/Copper Interconnect Patterns

Joo Hoon Choi and Chad S. Korach[z]

Department of Mechanical Engineering, State University of New York at Stony Brook, Stony Brook, New York 11794-2300, USA

Chemical mechanical polishing (CMP) can lead to nanoscale damage in films and surface features due to normal and lateral deformations of the surface. Defects arise due to the synergistic effects of chemical and mechanical mechanisms. This occurrence increases with severity as feature sizes are on the same order as abrasive polishing particles and materials decrease in stiffness, as with advanced low-*k* dielectrics. Here, relationships describing the response of normal and lateral surface deformations have been developed experimentally and from contact modeling. This is achieved by atomic force microscopy nanoscratching with diamond tips in a KOH environment to simulate CMP processing conditions. The deformations are related to the applied normal load, friction coefficient, film properties, and line densities. The deformations are observed to have critical loads of 1 and 5 μN associated with normal and lateral deformations, respectively, which are on the same order as actual CMP particle pressure estimates.
 [DOI: 10.1149/1.3243852]

Manuscript submitted May 31, 2009; revised manuscript received August 10, 2009. Published October 22, 2009.

There exists an ever increasing need in the semiconductor industry to reduce the size of an integrated circuit (IC) while improving its performance. This has been achieved by producing multilevel structures and using advanced materials.[1] With the use of layered structures, the formation of nonplanarized surface topography during fabrication is a challenge. Chemical mechanical polishing (CMP) has been developed intensively and has shown a dynamic growth, playing a key role in the semiconductor industry because it is not only an efficient planarization process but also an effective way of removing wafer surface defects. CMP has allowed the improved lateral circuit dimensions to minimize interconnect delay,[2] and the minimization process has been achieved by the transition from aluminum to copper metal interconnects and from traditional dielectric SiO_2 to low-*k* (LK) or ultralow-*k* (ULK) dielectric materials.[3] However, the adoption of porous LK materials has brought implementation problems, such as delamination of dielectric materials during CMP due to poor adhesion between layers, poor mechanical strength of porous LK interlayer dielectrics,[4] low thermal conductivity, and incompatibility with existing IC manufacturing processes.[5,6] The formation of surface defects on LK interlayer dielectrics during CMP affects local, near-neighbor structures as well as multilevel structures after subsequent process steps, leading to decreased reliability and performance degradation.

Many researchers have worked to investigate LK dielectric material delamination and wear.[7-14] Busch and Hosali[15] observed structural and chemical modifications of LK materials due to CMP operating conditions, whereas Balakumar et al.[16] performed CMP on Cu/SiLK single- and dual-stack nonpatterned wafers to study fundamentals of delamination during CMP, and Leduc et al.[17] measured the dependence of CMP-induced delamination on LK dielectric film stacks and established a relationship between delamination and the number of ULK dielectric layers.

In addition to the efforts to investigate delamination during CMP directly, much work has been accomplished to model CMP for process optimization. Models have been developed based on finite element analysis (FEM), contact mechanics theory, plasticity, and abrasion mechanisms to estimate the material removal rate during CMP.[18-26] Instead of observing CMP from a process level, many researchers have utilized scanning probe microscopy to investigate the fundamental responses occurring during CMP at the nanoscale, which leads to a better understanding and control of the CMP process. At the scale of the individual slurry, particle surface forces and potentials form a significant factor in agglomeration and material removal, and have been measured between oxidized silicon wafers and model polishing particles in the form of colloidal spheres attached to atomic force microscopy (AFM) cantilevers,[27] between silicon nitride (Si_3N_4) AFM tips and oxide wafers in KNO_3 electrolyte under pH environments of 3–11,[28] as well as between silica and silicon nitride AFM probes and polyurethane CMP polishing pads in KNO_3 solution with pH values from 4 to 10.[29]

Utilizing colloidal particles and AFM probes to measure lateral interactions and friction at the micro- and nanoscale to simulate an individual polishing particle has been a focus to identify slurry optimization and material removal. Silica microparticles have been attached to bare AFM cantilevers to measure friction on Si and silica substrates, and a dependence on pH [30] and surfactant concentration[31] as well as load conditions was observed. Material removal at the microscale was demonstrated using microscratch techniques to mimic particle interactions with substrates for Cu detachment,[32] and the strength of SiC/LK/Si layer stacks has been measured using microscratch to observe cohesive and adhesive failure of the layers.[33] Though microscratch techniques can successfully employ similar contact pressures as abrasive particles in polishing, size effects associated with the contact stress fields are not on similar orders as smaller, nanoscale measurements using nanoscratch techniques. The use of atomic force microscope probes has been employed to measure nanoscale tribochemical wear of sodium trisilicate glass substrates[34] and the material removal rate of aluminum as a function of pH and applied potential.[35] The determination of scratch loads necessary for plastic deformation of LK and copper films has been investigated using micrometer-scale diamond probe cantilevers.[36]

In this work, the goal is to measure the surface and lateral deformations of Cu/LK dielectric patterned wafers by the analog of a single CMP particle and to determine the loads that initiate defect damage to sample surfaces. This was achieved by using AFM nanoscratching in KOH to mimic the surface damage introduced during CMP. Surfaces were investigated with AFM and scanning electron microscopy (SEM) to observe the scratch depth and line deformation of patterns, respectively. Critical loads that initiate deformation were estimated for each structure, and the results can be used as a guide for determining preferred pattern ratios. A contact analysis is applied to understand the generation of stresses that drive the surface damage and relate to the materials and pattern densities.

Experimental

AFM cantilevers.— Because friction measurements on a patterned silicon wafer are subjected to a high load, it was necessary to have a probe that was highly resistant to wear and a cantilever that was stiff enough to apply large normal and lateral loads for scribing. Au-coated reflective triangular Si cantilevers with a diamond-coated probe tip (DCP20, NT-MDT) were used. The triangular cantilevers were 90 ± 5 μm long, 60 μm wide, and 2 μm thick, with typical

[z] E-mail: chad.korach@stonybrook.edu

spring constants of 48 N/m. Because the range of the spring constant provided by the manufacturer had a large variation, the cantilever spring constants were calibrated before performing experiments to know the applied load with precision during experiments.

Spring constants of triangular cantilevers (k_{tri}) were determined using the thermal tuning method.[37] The method was developed for a rectangular cantilever (k_{rect}); thus a correction for the triangular cantilever geometry was used ($k_{tri} = 0.764k_{rect}$), as determined by Stark et al.[38] from FEM. The basic concept of the thermal tuning technique is to measure displacements of a cantilever while the cantilever vibrates at its natural frequency due to thermal fluctuation of air surrounding it without the presence of an external force. The displacements are measured as a function of corresponding frequencies, and the spring constant of the cantilever can be determined by

$$k_c = 0.764\frac{k_b T}{A} \quad [1]$$

where k_c, k_b, T, and A represent the spring constant of the cantilever, the Boltzmann constant, the measured temperature in kelvins, and the area under the power spectrum-frequency curve, respectively. The atomic force microscope head and sample stage (NT-MDT SolverProM AFM) were isolated from the ambient laboratory environment by placement of a metal hood designed to thermally stabilize the experimental setup and to minimize acoustical interference. The vibration from the ground was isolated by an active vibration isolation system (Halcyonics Micro 40). The temperature was measured after thermal equilibrium was reached. The temperature inside the metal hood was measured by an internal thermocouple.

A script built in to the AFM control and analysis software was used to integrate the power spectrum-frequency curve and required cantilever sensitivity. Cantilever sensitivity, which relates cantilever deflection (in nanometers) to the photodiode signal change (in nanoamperes), was measured by force spectroscopy on a rigid sapphire substrate that was surface-cleaned with isopropyl alcohol and dried in laboratory air. The sensitivity was determined by averaging the slopes of five separate force spectroscopy curves at separate locations. Applied normal loads were calculated by multiplying the spring constant (k_c) by a distance that was measured from the force-displacement curve for a given photodiode signal change.

Lateral force calibration factors for the AFM cantilever were determined using the cantilever lateral sensitivity with the photodiode and the lateral (torsional) spring constant (k_{cL}) calculated by geometry.[39] Because k_{cL} was sensitive to the values of the elastic modulus and the thickness of the cantilever, the lateral spring constant measured from geometry might deviate from its actual value significantly. This was avoided by determining the value of the product $E \times t^3$, which is common to the normal and torsional spring constants,[40] measured from the normal spring constant determined by thermal tuning, where E is the elastic modulus of the cantilever (Si) and t is the cantilever thickness. Values for triangular cantilever torsional spring constants are considerably larger due to the inherent stiffness in the lateral direction and provide an increased accuracy.

The AFM probes and patterned substrates were observed using SEM (LEO Gemini 1500 SEM). The diamond coating (which was doped with nitrogen) was observed with SEM to measure the thickness of the coating and the radius of curvature of the probes (Fig. 1). The thickness was observed to estimate the degree of wear of diamond coating due to nanoscratch tests, and the radius of curvature was measured to estimate the stress applied by the diamond-coated probe. A backscattering detector with 20 kV and 8 mm working distance was utilized to image the diamond coating. The averages of the measured thickness and the radius of curvature were approximately 100 and 82 nm, respectively. Imaging of the pattern densities on individual substrates was also performed by SEM. After performing the nanoscratch tests, SEM was used to observe the AFM probes and the lateral deformation on the surface of the patterned substrates.

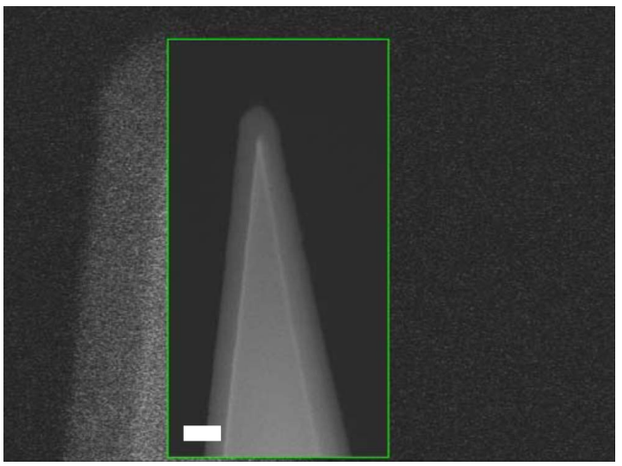

Figure 1. (Color online) SEM micrograph of a diamond-coated polysilicon AFM probe before scratching testing. Probe tip radius is measured as ~80 nm and coating thickness as 100 nm. Scale in figure represents 200 nm.

Materials: Cu/LK patterned wafers.— Patterned silicon wafers containing a polycrystalline copper serpentine line structure within an LK silica dielectric were used to provide all specimens (Fig. 2). Samples were diamond-scribed from 300 mm wafers into square specimens 10 × 5 mm. Copper interconnect and dielectric film patterns had variations in line width and in spacing ranging from 80 to 235 and from 80 to 245 nm, respectively. To assist in normalizing the patterns, a pattern density (L) is defined by the ratio of dividing a copper interconnect width (l_{Cu}) to the sum of the copper interconnect and dielectric film widths ($l_{Cu} + l_{LK}$). SEM was used to measure the widths of the copper interconnect and dielectric films and are presented along with the pattern densities in Table I.

Two different carbon-doped oxide LK dielectric materials ($k_A = 3.05$; $k_B = 2.50$) taken from separate patterned wafers were compared. Mechanical properties of the two dielectrics (see Table II) varied more for nanohardness than for the elastic modulus, both measured by nanoindentation, and were considered to be due to the change in porosity. The porosity differed by a factor of ~3 from film A to B, a clear indicator of the change in dielectric constant of the film.

AFM force lithography.— To perform nanoscale scratch testing on the patterned substrates, AFM force lithography was utilized, which is a technique that scans a prescribed region of a sample with

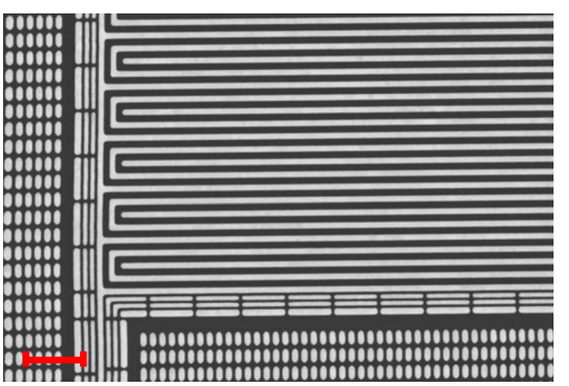

Figure 2. (Color online) Patterned silicon wafers containing copper serpentine line pattern within an LK dielectric. The approximate region of testing was in the center of the micrograph. Scale bar represents 2 μm.

Table I. Widths of the copper and dielectric materials within each structure and the corresponding pattern densities.

Structure	Width (nm)		Dielectric film	Pattern density
	Copper	Dielectric		
1	235	142	A	0.623
2	223	246	A	0.476
3	124	41	A	0.751
4	81	82	B	0.497

a controlled load and geometry. The method can be considered as a "write" technique and can be used for a variety of applications when integrated with fluid reservoirs and heated probes. By recording the cantilever deflection and torsion signals while scanning, lateral forces and coefficients of friction (COFs) can be calculated. Friction force or lateral force measurements are similar techniques that apply normal loads orders of magnitude smaller. Here, samples were mounted in an open wet cell, where the force lithography was performed on specific line patterns found on the surface with a diamond-coated probe tip connected with a high stiffness cantilever. After completing the spring constant measurements and the sample preparation, the sample was mounted on a wet cell and the calibrated cantilever was installed on a glass prism holder. KOH (pH 9.21) filled the wet cell, completely submerging the sample and the cantilever. Patterns of interest were identified using an optical microscope attached to the atomic force microscope, and a series of scans was performed to locate the pattern. The time to install, calibrate, and perform nanoscratches was controlled at 1 h exposure time in KOH. Force lithography was used to produce scratches perpendicular to the serpentine line patterns. The same location (see center of Fig. 1) in the line patterns was chosen for every sample to remain consistent and also to provide a guide to locating the nanoscratches after testing. A wide span of applied normal loads was applied to determine the minimum load to plastically deform the surface and to obtain measurable surface deformations such as the scratch depth and lateral deformation of patterns as a function of applied normal load. For all lithography scans, the scratch length was 2 μm and the scribing speed of the AFM probe was 0.64 μm/s. The separation between scratches was 1 μm. The speed of AFM-based nanoscratching is many orders of magnitude lower than a commercial CMP process, which typically has a linear velocity of 1 m/s. The nanoscratch tests presented here represent an upper bound to defectivity because as the speed increases, the friction may decrease due to lubrication effects. Due to potential wear of the diamond-coated probes, a single cantilever was used for the force lithography of two patterns. After completion of the force lithography, the sample surfaces were scanned in an intermittent contact mode with a separate imaging cantilever to observe surface deformations made on the copper interconnects and the dielectric films. This allowed observations and analysis of the three-dimensional (3D) topography and profiles of the scratches to measure the depth and corresponding pileup to investigate relationships between the applied loads and scratch depths. In addition, SEM was used to image lateral deformation of copper interconnects and dielectric films due to lateral forces applied during scratching. AFM, though effective in observing changes in topography, was unable to determine lateral deformation of line patterns.

Table II. Properties of dielectric film materials used in this work.

Dielectric film	Elastic modulus (GPa)	Hardness (GPa)	Porosity (%)
A	11.1	2.1	6.7
B	8	1.4	25

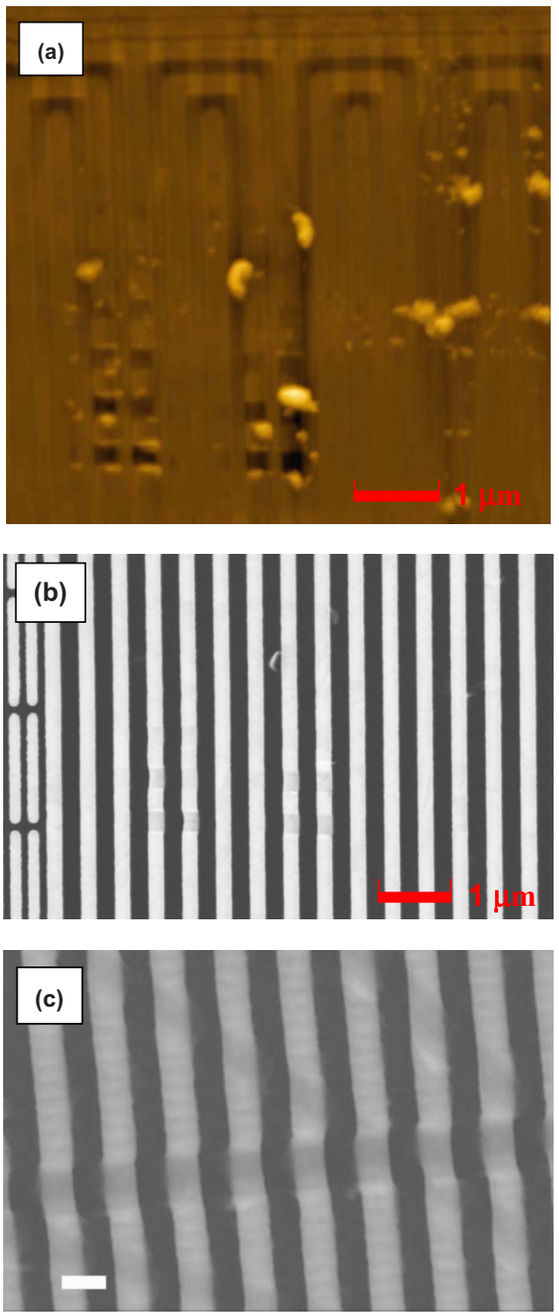

Figure 3. (Color online) (a) AFM topography image of a scratched line on structure 2. Peak-to-valley height of image is 200 nm. (b) SEM micrograph of the same structure. (c) Nanoscratch defect on structure 2. Scale bar represents 300 nm.

Results

Measurement of scratch deformation.— The surface topography after testing was measured with an atomic force microscope in intermittent contact mode. Imaging was done immediately after testing to avoid sample surface contamination within the wet cell. Intermittent contact mode is used so that damage does not occur due to topography scanning with a high spring constant cantilever. An AFM topography image is shown in Fig. 3a, where a series of nanoscale scratches was performed across the line pattern with increasing loads from top to bottom in the image. In comparison, the same sample surface is seen in Fig. 3b, as imaged in the SEM micrograph.

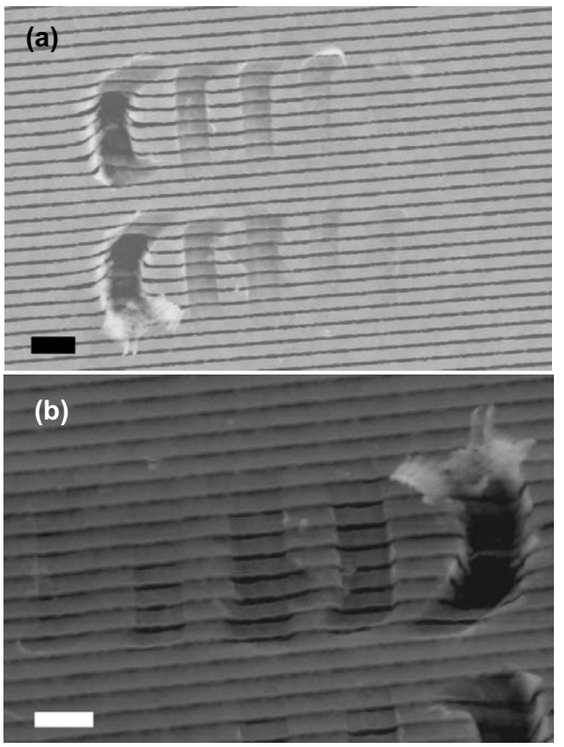

Figure 4. (a) Array of nanoscratch defects observed by SEM on structure 4 from a direction normal to the surface. Scale bar represents 500 nm. (b) Glancing angle SEM of the same nanoscratch array. Scale bar represents 400 nm.

The dark regions of the serpentine line structure represent the dielectric material, where the light regions are the copper. Figure 3c gives a higher resolution example by SEM of a single nanoscratch over the Cu/LK structure. Normal and lateral deformations are present at the Cu/LK interfaces. Using an atomic force microscope, the copper lines showed a positive height difference of ~2 nm from the dielectric film. Lines were verified with SEM and energy-dispersive X-ray spectroscopy by determining the chemical composition as a function of spectral location. Another series of nanoscale scratch defects shows the progression in damage with increasing load (right to left in Fig. 4a). Delamination is observed for the highest loading, and unobservable surface changes are made for the lowest load. The extent and depth of the damage is shown in Fig. 4b, with a clear abrupt transition between the two defects on the far right of the micrograph.

AFM topography data were analyzed along the scratching direction and perpendicular to the scratches. For the profiles along the scratch directions, the deformation of copper interconnects (see Fig. 5) and dielectric films was analyzed simultaneously to measure average scratch depth (δ_c) for a given applied normal load. Surface profiles perpendicular to the scratches on the copper interconnects and dielectric films were measured separately to observe the effect of applied normal loads on the two materials. The same analysis was repeated for structures with different line densities to observe the effect on the deformations.

It was observed that the deformation of the dielectric film was negligible because the deformation of the film was on a similar magnitude as the roughness measured from the reference profile. However, a noticeable variation in scratch depth was observed on the copper interconnect, and this indicates that the dielectric film is less susceptible to damage due to the lateral load compared to the copper interconnect.

Figure 6 shows the residual depth in the copper regions measured

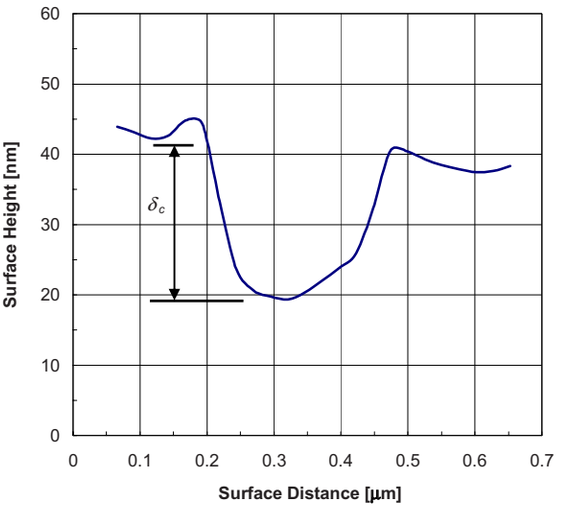

Figure 5. (Color online) AFM cross-sectional profile of scratch depth (δ_c) for ~16 μN load on structure 2.

from scratches made on structure 2 for applied normal loads in the range of 10–19 μN. To remove the initial surface topography from the calculations, a reference profile along the intact Cu/LK films was used to measure the height variations of the intact copper regions. As one would expect, the scratch depth increased as the applied normal load increased. By extrapolating the regression line down to the abscissa, the critical load, which is the normal load that initiates the plastic deformation of the surface, was estimated to be 8.7 μN. This estimation is an indicator of the maximum normal load that is necessary to create surface defects.

Pileup of the Cu material due to permanent deformation was observed by AFM for the postscratch analysis to occur in small amounts at low loads and larger magnitudes for higher loads. The magnitude of the pileup height was smaller than that of the scratch depth; however, the highest applied loads studied showed an almost one-to-one correspondence with the copper permanent deformation. The formation of pileup is consistent with what others have observed for microscale scratch tests on copper surfaces.[25,32] Thus, for high down forces, the pileup could represent an additional surface defect generated in CMP that can form an out-of-plane topography affecting subsequent deposited surface layers.

During scanning, lateral friction forces were determined simultaneously by measuring the torsional signal from the AFM photodiode

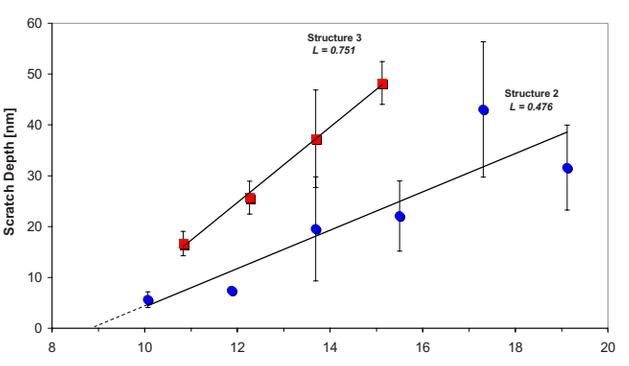

Figure 6. (Color online) Copper line permanent scratch depth measured by AFM as a function of a normal load for pattern structure 3 (L = 0.751) vs structure 2 (L = 0.476). Dashed regression line indicates a critical load at the x-intercept.

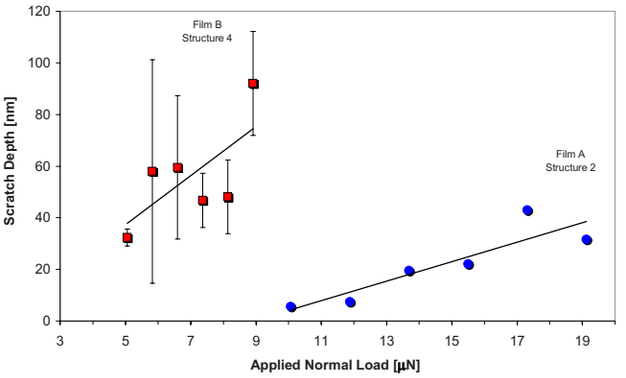

Figure 7. (Color online) Copper scratch depth as a function of a normal load for two LK dielectric films with different mechanical properties. Hardness and elastic modulus of film A > film B.

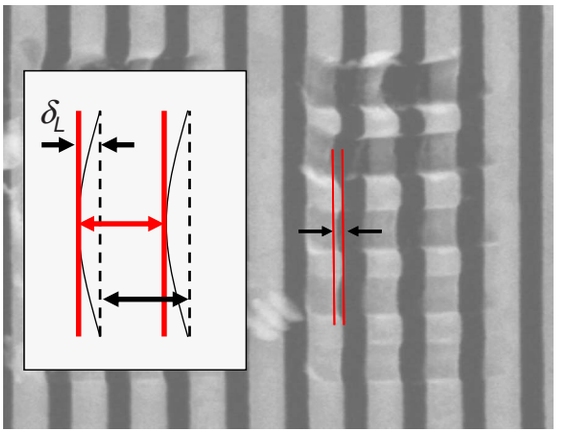

Figure 8. (Color online) Measurement of lateral line deformation (δ_L) performed with SEM of nanoscratches on a wafer surface. δ_L measurement distance is given in the inset.

and multiplying by the lateral force calibration factor determined before testing. COFs (μ) were calculated by dividing the lateral forces by the applied normal forces and were in the range of 0.3–0.6 for all tests. These values are within the range of globally measured COFs from commercial scale CMP equipment. Adhesion forces were not utilized in calculating normal forces or COFs because the high normal contact loads (order of micronewtons) were dominant. Variations in lateral forces from the dependency of the structure dimensions were not observed, though changes in the COF were seen in increased normal loads.

The effect of the pattern line density was observed by comparing the scratch deformation results for structures 2 and 3, which are both samples with dielectric film A. Structure 2 (L = 0.467) and structure 3 (L = 0.751) were chosen so that the effect of a wider copper interconnect line with respect to the dielectric width could be observed. In Fig. 6, the scratch depths of both structures are presented as a function of applied normal load. The critical loads (i.e., the loads to initiate a permanent deformation) for structures 2 and 3 were estimated to be 8.8 and 8.7 μN, respectively, implying that both structures began to incur a permanent deformation at a similar normal load. The results indicate that structure 2 requires a higher normal load to obtain the same deformation as structure 3 over the load range. This is quantified by the slope m of linear regression lines (m = 0.0038 and 0.0074 for structures 2 and 3, respectively) in Fig. 6. The results show a smaller slope for the lower density structure 2, implying that a lower density decreases the scratch deformation. This may be explained by the confinement of the copper line within the LK dielectric film and is addressed in the Discussion section.

Two structures that had a similar line density but were composed of different dielectric materials were tested with the AFM nanoscratch technique. The elastic modus and nanohardness of the two dielectric materials are presented in Table II. Copper line scratch depth response to normal loads is shown in Fig. 7 and indicates that the weaker dielectric film B is far more susceptible to plastic deformation than dielectric film A. A regression analysis of the data shows a larger slope for dielectric film B than that in dielectric film A, indicating that structure 4 is more susceptible to deformation for similar applied loads. The critical load to initiate deformation in structure 4 (film B) was estimated to be 1.1 μN, compared with 8.8 μN in structure 2 (film A). The results show that film B provides less constraint to the contact loads and stresses during scratching, which is due to the lower stiffness and hardness of the material.

Measurement of line deformation.— Lateral line deformation (δ_L) is measured by determining the displacement of the Cu/LK interface from the SEM micrographs. An illustration of how the line deformation of a pattern is measured is presented in Fig. 8. Measurements on the micrographs were made using digital imaging software. The distance between the intact (outside the scratch) and the deformed interface within the scratch is measured to quantify the deformation. Measurements of the deformed interface are made at the centerline of the scratch direction because the maximum contact stresses that yield the materials are highest at the center of the probe.

Lateral deformations of the copper and dielectric line patterns for structures 1 and 2, which had different line densities (L = 0.623 and L = 0.476 for structures 1 and 2, respectively), were obtained after scratches were performed using SEM. Dielectric film A was present in both tested patterns. Measurement techniques were followed as described above. The high Cu density pattern (structure 1) was observed to exhibit less resistance to bending due to a lateral applied force (see Fig. 9). The critical normal loads for initial deformation were determined by the intercept of the regression line with the x-axis and were estimated to be 5.3 and 10.6 μN for structures 1 and 2, respectively. An increased slope of the linear regression line for structure 1 (m_{1L} = 0.0054) indicates that the lateral deformation requires a smaller load to achieve the same compared with structure 2 (m_{2L} = 0.0032); thus, the thinner dielectric film width between copper lines increased the amount of observed line deformation. The decreased constraint of the dielectric thickness between copper lines of the same width allowed lateral forces translated into shear stresses to shift the pattern. This can be considered as a two-dimensional (2D) element of the material, where the free surface contains shear traction and the lower surface is assumed to be constrained to the substrate. The extent of the lateral deformation into the surface has not been observed, though the materials did remain

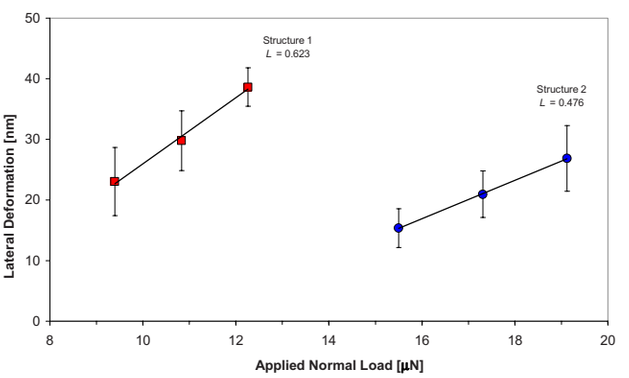

Figure 9. (Color online) Cu/LK lateral line deformation for pattern structure 1 (L = 0.623) vs structure 2 (L = 0.476).

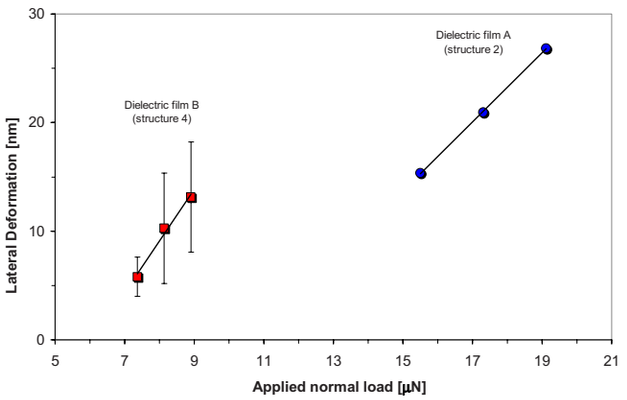

Figure 10. (Color online) Effect of film materials on Cu/LK lateral line deformation for similar pattern density structures.

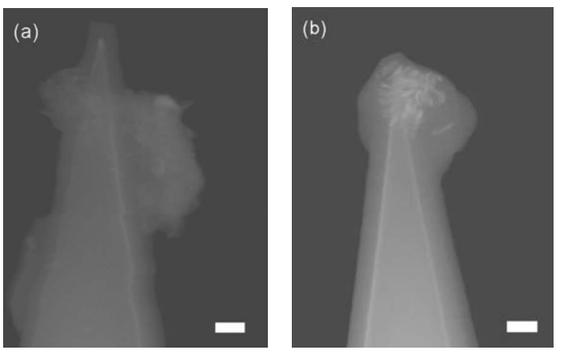

Figure 11. SEM micrographs of diamond-coated AFM probes after nanoscratch testing (scale bar represents 200 nm in both). (a) A change in the probe tip curvature after scratch testing is shown, and [(a) and (b)] debris formation from surface machining and wear on the tip ends . Diamond coating is shown to remain intact after testing. (b) A longer scan distance (80 μm) was used with probe tip, increasing the wear debris.

adhered to the substrate as long as applied loads were not high enough to cause delamination of the pattern, which was observed at very high loads. Because the normal surface displacements measured are on the order of 10–40 nm and the vertical film thickness is on the order of 500 nm, the contact stress field is a local phenomenon and remains in the patterned film. For thinner films or different size indenter tips, results are affected by these size effects due to the contact stress field in the subsurface being related to the film thickness through a substrate effect and the indenter size by a contact pressure similarity.

The effect of dielectric film material properties on lateral line deformation was observed in structures 2 and 4, which had a similar line density but different dielectric film materials (A vs B). Figure 10 shows that a difference in the dielectric film material properties has a significant effect on the amount of line deformation. Dielectric film A was close to 2 times more resistant to line deformation than the more porous film B. This effect can be considered by an element of material that is effectively thinner due to the property decrease. Similar to the effect a decreased dielectric line thickness had on an increased line deformation, the property decrease has a similar effect on the response. Critical loads to initiate the line deformation are determined as 6 and 10.6 μN for films B and A, respectively. The results show that both line density and dielectric material properties affect the lateral deformation of the patterned Cu/LK structures.

SEM imaging of AFM probes.— After performing nanoscratch tests, the used probe tip was observed again with SEM to determine alterations in the tip geometry. The SEM micrographs of the probe tip show a significant change in the geometry after scratch testing. Figure 11a shows a tip after scratch testing where the probe geometry has increased locally at the end of the tip. This change in geometry corresponds to indentation depths observed during scratching and indicates that a larger probe radius was in contact with the surface than what was originally measured. The probe radius of curvature is estimated to increase at the apex to 500 nm. However, even though the tip has shown geometrical changes, the diamond coating remains intact, as observed in SEM (Fig. 11a). This indicates that an initial running in occurred at the end of the probe, before a stable radius of curvature was obtained, and could have occurred during the initial surface imaging in the alkaline KOH solution. This result also demonstrates that the diamond like carbon (DLC) coating has a coherent bond with the polysilicon probe tip, and the forces applied during loading do not cause coating delamination from the tip. This is a significant result because a knowledge of the probe surface properties (here DLC) is necessary to have a clear understanding of the substrate response. Debris from surface machining and wear is formed on the tip ends. As shown in Fig. 11a and b, debris became attached to the probe surface after scratch testing. In both instances, the probe tip is observed to protrude from the debris mass; therefore, the DLC probe is in direct contact with the substrate during scratch testing. What is unique is that material removal is evident, and that nanoscale ribbons (or long chips) of Cu and LK films adhered together are observed, indicating a good cohesion between the Cu and LK lines. Figure 11b represents a probe that was used for significantly longer scratch distances (~80 μm) than the results reported here. The significant debris formation occurred in the large normal load cases that were performed, and it is not clear if this is due to adhesive delamination failure of the Cu layer. There is evidence that at high loads, the delamination of Cu from the LK substrate was observed.

Discussion

Scratch mechanics.— To analyze the effects of applied load, material properties, and line density on the experimentally observed surface and lateral deformations, the scratch mechanics is modeled with a quasi-static sliding contact model. The problem of a sliding contact between the particle analog (probe tip) and the substrate is described in Fig. 12, where the *y*-direction is taken out of plane. Surface deformation is governed by the mechanical properties of the materials and the boundary conditions due to the free surface, substrate, and line interfaces. During contact, a complex stress state that is related to the material deformation is produced. Considering a half-space of a homogeneous linear material, the contact stresses on the surface and within the subsurface are calculated following Hamilton and Goodman[41,42] for a 3D sliding contact (with a circular

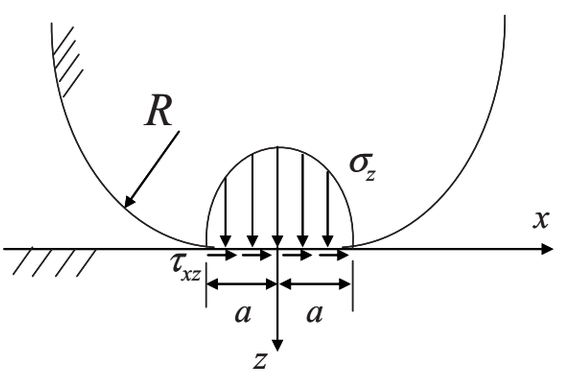

Figure 12. Description of the scratch mechanics contact model between the probe tip and substrates. Traction (pressure) is applied in the normal and tangential directions at the circular contact area, which has a diameter of 2*a*. The *y*-direction is taken out of plane.

contact area of radius a), where the boundary conditions inside the contact circle are based on the Hertzian pressure relation for the normal direction (z) stress

$$\sigma_z = -\frac{3P}{2\pi a^3}\sqrt{a^2 - r^2} \quad [2]$$

and the shear traction relation

$$\tau_{zx} = -\frac{3F}{2\pi a^3}\sqrt{a^2 - r^2} \quad [3]$$

with the condition that $F = \mu P$, where F is the friction force, P is the normal load, ν is Poisson's ratio, E is the Young's modulus of the material surface, and $r^2 = x^2 + y^2$. The remaining four components of stress represented as combined stresses based on superposition of the normal and shear traction distributions at the surface ($z = 0$) and within the contact area ($r < a$) are given by

$$\sigma_x = \frac{3P}{2\pi a^3}\left[\frac{1}{r^2}\left\{\frac{y^2 - x^2}{r^2}\left[\frac{1-2\nu}{3}\{(a^2 - r^2)^{3/2} - a^3\}\right] - (x^2 + 2\nu y^2) \times (a^2 - r^2)^{1/2}\right\}\right] + \frac{3F}{2\pi a^3}\left[-\frac{\pi x}{2}\left(\frac{\nu}{4} + 1\right)\right] \quad [4]$$

$$\sigma_y = \frac{3P}{2\pi a^3}\left[\frac{1}{r^2}\left\{\frac{x^2 - y^2}{r^2}\left[\frac{1-2\nu}{3}\{(a^2 - r^2)^{3/2} - a^3\}\right] - (y^2 + 2\nu x^2) \times (a^2 - r^2)^{1/2}\right\}\right] + \frac{3F}{2\pi a^3}\left[-\frac{3\pi\nu x}{8}\right] \quad [5]$$

$$\tau_{xy} = \frac{3P}{2\pi a^3}\left[\frac{xy(1-2\nu)}{r^4}\left\{-(a^2 - r^2)^{1/2}r^2 - \frac{2}{3}(a^2 - r^2)^{3/2} + \frac{2}{3}a^3\right\}\right] + \frac{3F}{2\pi a^3}\left[\frac{\pi y}{4}\left(\frac{\nu}{2} - 1\right)\right] \quad [6]$$

$$\tau_{zy} = 0 \quad [7]$$

The maximum stress for COFs greater than 0.3 (for $\nu = 0.3$) resides at the surface. From the lateral and normal forces determined by the AFM cantilever during testing ($\mu \sim 0.3$ to 0.6), assumption of at least $\mu = 0.3$ between the diamond probe tip and the surface materials (copper and an LK dielectric) is made in the analysis.

Contact stresses normal to the surface are calculated from Eq. 2, where the maximum contact stresses (pressure) for the copper and dielectrics (A and B) are located at the center of the contact ($r = 0$) and are estimated to be 4.20, 0.926, and 0.745 GPa, respectively, for a normal load of $P = 8$ μN, which is chosen as an approximation for the highest load to initiate the deformation observed experimentally. The contact radius a was calculated using the values given in Table II with $\nu_{LK} = 0.17$ and in addition for diamond ($E_{diamond} = 1141$ GPa and $\nu_{diamond} = 0.07$) and copper ($E_{Cu} = 110$ GPa and $\nu_{Cu} = 0.3$) by the Hertzian contact analysis

$$a = \left(\frac{3PR}{4E^*}\right)^{1/3} \quad [8]$$

$$\frac{1}{E^*} = \frac{1 - \nu_1^2}{E_1} + \frac{1 - \nu_2^2}{E_2} \quad [9]$$

which relates the load, geometry, material properties, and the contact area.[43] For the diamond-coated AFM probe, the radius of curvature was assumed to be 500 nm because of the tip wear during experiments. The point of initial yielding occurs at a fraction of the maximum contact pressure[44] and is approximated to occur when the mean pressure equals a fraction of the material hardness. Compared with the hardness of copper, which is taken as ~1 GPa, the material is expected to incur permanent deformation when a yield criterion of the material is exceeded. It is evident from the calculated theoretical normal contact stress that the pressures never obtain magnitudes of this order in these materials. Indeed, these values are for monolithic films and as such are not affected by neighboring materials of different properties, notably the elastic modulus in this case, and the introduction of a composite structure is the cause for the initiation load to achieve such a large value. This is addressed in the next section.

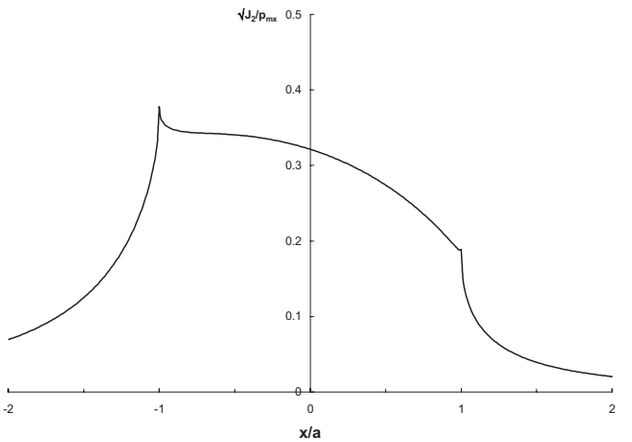

Figure 13. Distribution of the stress $\sqrt{J_2}$ on the surface ($z = 0$) centerline ($y = 0$) for $\mu = 0.3$ and $\nu = 0.3$. The maximum value of $\sqrt{J_2}$ occurs at the trailing edge of contact ($x = -a$).

To realize the effect of the normal and tangential pressures together, it is more relevant to represent the stress in a combined state with the von Mises yield parameter

$$J_2 = \frac{1}{6}[(\sigma_x - \sigma_y)^2 + (\sigma_y - \sigma_z)^2 + (\sigma_z - \sigma_x)^2] + \tau_{xy}^2 + \tau_{zx}^2 + \tau_{zy}^2 \quad [10]$$

On the surface centerline ($z = 0$, $y = 0$), $\sqrt{J_2}/p_{mx}$ is plotted in Fig. 13. As the COF increases, surface stresses are more dominant than subsurface stresses, and significant yielding occurs at the surface.[42] The center of the trailing edge of the probe represents the critical stress location, as indicated in Fig. 13. When the COF is less than 0.3, the material is predicted to initiate yielding in the subsurface. When the values of J_2 are greater than or equal to a critical stress value, yielding would be expected. This is given by

$$\sqrt{J_2} \geq \frac{Y}{\sqrt{3}} \quad [11]$$

For $\sqrt{J_2}/p_{mx} = 0.378$ (assuming $\mu = 0.3$), then $p_{mx} = 2.65\sqrt{J_2}$. Taking $\sqrt{J_2} = Y/\sqrt{3}$, where Y is the yield strength in simple tension, for surface yield $p_{mx} = (2.65/\sqrt{3})Y$. Considering the mean pressure of the normal contact, where $\bar{p} = \frac{2}{3}p_{mx}$, then $\bar{p} = \frac{2}{3}(2.65/\sqrt{3})Y$. Assuming Meyer's hardness relationship for the materials, $Y \approx H/3$, then the mean pressure is given as $\bar{p} = \frac{2}{9}(2.65/\sqrt{3})H$. The load for yielding is rewritten using the mean pressure definition of the load-to-area ratio

$$P = \pi a^2 \frac{2 \times 2.65}{9\sqrt{3}}H \quad [12]$$

The contact radius a is measured experimentally to range from 100 to 150 nm. For $H \sim 1$ GPa (the LK dielectric and Cu have similar orders of hardness values) the load to cause surface deformation during sliding is measured to be 10.7 μN. Equation 12 can be rewritten using Eq. 8 as

Table III. Critical load necessary to initiate plastic deformation in the Cu/LK substrate as a function of COF (μ) for effective modulus (E^*) values associated with structures 2 and 4.

	P_{cr} (μN)	
μ	(E^*_{eff} = 12.5 GPa)	(E^*_{eff} = 44.1 GPa)
0.1	6.51	52.10
0.2	2.38	19.05
0.3	1.10	8.78
0.4	0.59	4.71
0.5	0.35	2.81
0.6	0.23	1.80
0.7	0.15	1.22
0.8	0.11	0.87
0.9	0.08	0.64
1	0.06	0.48

$$P = \pi^3 R^2 \frac{H^3}{E^{*2}} 0.0221 \quad [13]$$

For the LK dielectric, with E = 8–10 GPa and H = 1–2 GPa, as measured from nanoindentation, the range of load is P = 2.7–13.7 μN. Clearly, because the Cu lines have a modulus that is an order of magnitude greater and a similar hardness (~1 GPa), the load necessary to yield the Cu is much lower. This leads to the variation in normal surface deformation between the copper and LK lines observed in the postscratch AFM scans (see Fig. 3a). As the applied normal load was increased, the deformation difference became even more significant. As discussed above, the absolute values of the critical loads do not follow the model because of the interaction between materials; hence Eq. 13, which is based on monolithic material property assumptions, is inaccurate, and this is addressed by considering an effective film modulus. If E^* is replaced by E^*_{eff} in Eq. 13, the values of E^*_{eff} are estimated to be 12.5 and 44.1 GPa for critical loads of 1.1 and 8.8 μN. Based on the effective moduli calculated above, the values of normal load to yield the materials as a function of COF are listed in Table III, showing that the critical load decreases with the increase in COF. Parameters used in the model and in subsequent sections are found in Table IV.

The results can be compared with those of Saka et al.,[36] who performed microscratches on copper and LK dielectric blanket films in a dry environment using a plowing scratch model. Contact stresses from our experiments were in the range of 200–300 MPa, which were lower than those from the microscratch tests of Saka et al., where contact stresses were estimated from their data to be ~700 MPa. Also, the values reported here represented approximately the yield stress of the materials for the load range not including delamination of the structure. In CMP abrasive particle contact, normal loads in the range of 500–700 nN [31] and particle sizes ranging from 25 to 100 nm yield mean pressures at the abrasive particle contacts estimated as 1.5 GPa and larger, though exact knowledge of per abrasive particle load is not definitively known and is typically estimated based on geometric assumptions of the pad asperities and particle diameters. The ability of standard polyurethane polishing pads to withstand contact pressures of orders above the polymer yield stress and to not partially absorb the load by substrate contact is unclear and potentially accounts for load support altering the per particle load.[45] Here, we have reported contact pressure-based analysis necessary to deform the line structures that can be utilized regardless of the load.

Table IV. Parameters used in the data analysis with the scratch deformation model.

Parameter	Symbol	Values
Critical normal load	P_{cr}	1.1–10.6 μN
COF	μ	0.3
Modulus, Cu	E_{Cu}	110 GPa
Poisson ratio, Cu	ν_{Cu}	0.3
Hardness, Cu	H_{Cu}	1 GPa
Modulus, diamond	$E_{diamond}$	1141 GPa
Poisson ratio, diamond	$\nu_{diamond}$	0.07
Poisson ratio, LK	ν_{LK}	0.17
Tip radius of curvature	R	500 nm
Structure 2 (Fig. 6) slope	m_2	0.0038 nm/μN
Structure 3 (Fig. 6) slope	m_3	0.0074 nm/μN
Structure 1 (Fig. 9) slope	m_{1L}	0.0054 nm/μN
Structure 2 (Fig. 9) slope	m_{2L}	0.0032 nm/μN

Normal surface deformations.— The critical loads to yield normal surface deformations of the Cu lines observed and described in the previous section are not only a function of the Cu material properties but the overall interaction between the LK regions and the Cu lines. The effect of the LK on the copper deformation can be considered in the sense of an effective modulus of the patterned composite film (LK and Cu) with effective modulus E^*_{eff}. The normal load necessary to yield a film of bulk Cu only, as determined from Eq. 13, is much lower (~15 nN) than the applied loads observed in this work necessary to create permanent deformation in the Cu films. This effect is due to the introduction of the LK film material. Because the LK elastic modulus is an order lower than Cu, the load to yield is larger (as seen above) for similar geometries and film hardness values. Due to this effect, the concept of an effective modulus utilizes the extent of the ratio between Cu and LK materials. Considering the effect of copper line density in the film, the effective modulus can be calculated for the critical load of 1.1 μN (for L = 0.751) using a range of radius of curvatures (R = 100–500 nm) and H ~ 1 GPa to be 2.5–12.5 GPa. The unreasonable values of an effective modulus below a film modulus of 8 GPa are believed to be due to tip geometry. It is likely that locally, beyond what has been measured with SEM, the tip has worn to a larger radius of curvature at the apex, hence yielding a tip radius closer to the value of 500 nm. To compare the effects of different line densities, the slopes of the permanent deformation depth vs applied load (Fig. 6) are computed, where the slopes are m_2 = 0.0038 and m_3 = 0.0074 for L_2 = 0.476 and L_3 = 0.751, respectively. The results indicate that a similar critical load is necessary for permanent deformation to initiate (~8.8 μN), though the slopes of the two curves are distinctly different. A ratio of the slopes can be related to the ratio of the critical loads for each structure at a similar permanent displacement, where the effective modulus of each structure is considered an independent variable

$$\frac{m_3}{m_2} = \frac{P_2}{P_3} \propto \frac{(E^*_{eff,3})^2}{(E^*_{eff,2})^2} \quad [14]$$

The value of $\sqrt{m_3/m_2}$ = 1.4 can be compared with the ratio of the line densities for the two structures, L_3/L_2 = 1.58. The good correlation between the slopes of the copper permanent deformation curves and the line density gives a predictor of the extent of the copper deformation. This result indicates that even though the copper permanent deformation is a local effect in the copper portion of the structure, the LK material provides a constraint to the copper line. The ratio of the line density can represent a ratio of distances from the copper to the nearest LK interface; as this distance varies, so does the constraint on the copper deformation. Thus, the ratio of line densities scales the effective film moduli.

The effect of different LK film mechanical properties on the normal surface deformations presents again a linear relationship between permanent deformation and applied normal load, though there exist different locations of the intercepts with the zero displacement axes. These values represent the critical loads necessary to initiate permanent deformation. For the weaker, higher porosity film B (E

= 8 GPa, H = 1 GPa), the copper exhibits permanent deformations at lower loads than film A (E = 11 GPa and H = 2 GPa). Intuitively, the weaker film exhibits a higher compliance and allows the copper to permanently deform more readily, though the intriguing relationship is that the curves do not converge to a consistent value for initiation loading. Because the critical loads are experimentally measured to have a ratio of 8:1 (film A:film B), taking again the ratio of Eq. 13 for both films, though assuming in this case that the film modulus is of similar order, the ratio of the film hardness values becomes the dominant difference between the two LK film materials. Because the hardness goes as H^3 in Eq. 13, the ratio of the hardness is related to the critical load by

$$\frac{P_{\mathrm{cr,A}}}{P_{\mathrm{cr,B}}} \propto \left(\frac{H_{\mathrm{A}}}{H_{\mathrm{B}}}\right)^3 \qquad [15]$$

When $H_{\mathrm{A}}/H_{\mathrm{B}} \sim 2$ is substituted in Eq. 15, this yields a ratio of the critical loads $P_{\mathrm{cr,A}}/P_{\mathrm{cr,B}} = 8$, which demonstrates that the hardness ratio provides a relationship between the critical loads. A slope change associated with the different LK films is observed, though the pattern densities are similar. This may be due to the variation in the LK film modulus; when considering an effective film modulus, the value is affected by both the Cu and LK material properties, which may disproportionately affect the relationship between the normal load and permanent deformation. Therefore, the normal surface deformation is more dependent on LK film hardness, which is a stronger predictor of plastic yield when comparing film materials, and the response slope is related to the line density for the same LK films.

Lateral surface deformations.— As seen in Fig. 3 and 4, lateral surface deformations are semicircular, with maximum deformation occurring along the centerline of the scratch. This follows the contact stress analysis and the assumption that the material yields at a critical stress, which predicts that the highest stress occurs at the center region of the contact. It is also observed that there is no separation between the copper and LK dielectric line structures until significant plastic deformation and delamination occur. Even in this case, there is evidence from SEM analysis that material removal occurs as a single "chip" (see Fig. 4 and 8) with intact copper and LK regions. This result indicates a strong bond between the materials and the adhesion of the films to the underlying substrate. The lateral deformation follows the same response to loading, as described in the previous section. The contact stresses generate a maximum stress state (J_2) in the material, which can lead to yielding based on a specified criterion, though for the lateral deformations, the surface-driven yield is the dominant mechanism to create the yielding of the Cu and LK interfaces. The lateral deformation is more affected by the line spacing and widths than the normal deformation. As the probe traverses one domain to the next, the stress field interacts with the domain interface. The problem of a normal shear traction boundary condition at a bimaterial interface has been studied by Bogy.[46,47] When approaching a stiffer domain in a bimaterial, the interface deforms less. The mismatch between the two-material stiffness governs the surface deformation of the interface. As the domain widths are made finite, the effect of the Cu stiffness lowering the load to yield the surface becomes more pronounced with a higher Cu line density, which was experimentally observed. An increase in the dielectric spacing (i.e., a decrease in Cu density) leads to less lateral surface deformation and the bending of the domain boundary. By observing the slope of the two lines found in Fig. 9, the square root of the ratio ($\sqrt{m_{1\mathrm{L}}/m_{2\mathrm{L}}} = 1.3$) is used again as a scaling factor for the effective modulus. When compared with the line densities of the two patterns, the ratio of the structures is $L_1/L_2 = 1.31$. This result is explained by the lateral deformations being more strongly tied to the interface stiffness than the normal deformation of Cu. For narrower LK linewidths, which contain the more compliant but harder dielectric, the surface deformation increases, which can be considered as the constraint of the entire LK line decreasing, acting similar to a 2D fiber found in reinforced polymer composites.

Because the lateral surface deformations are more intrinsically associated with the stiffness of the Cu/LK interface, the effects of the LK material are more pronounced. If this is the case, then both the film hardness and the modulus must be considered because the deformation is a local phenomenon and is affected by both. The critical normal loads to initiate the lateral surface deformation are observed to be 6 and 10.6 μN for films B and A, respectively. Taking the LK properties from Table II and using both hardness and modulus as the independent variables, ratios of the critical loads can again be obtained. Using the measured mechanical properties, the ratio is ~1.9, where the experimentally measured value is ~1.8. This result indicates the significance of considering both LK mechanical properties in the estimate of the surface deformation.

Another point is the tensile stress at the trailing edge of the contact, which can be estimated for the observed experimental cases using Eq. 4 with $y = 0$, $x = -a$. This stress is a major contribution to the lateral surface deformations present on the sample and is estimated to be 446 and 529 MPa for the elastic moduli of films B and A, respectively, at the minimum critical load for initiation. The interfacial strength in the sliding normal direction (which represents an opening load) is therefore at least this value for the Cu/LK interface. This is an important aspect in surface-driven fractures of thin films, which can occur in brittle materials. Here, surface cracking was not observed. The extent of the lateral surface deformation is unknown at this point, but because the maximum stress state occurs at the surface, it is believed that the deformation is confined to the near surface of the film, though this will be investigated in the future.

Environmental effects on contact conditions.— All tests reported were carried out as explained in a KOH solution with pH 9.2. The value was chosen to simulate to a reasonable degree the contact conditions observed during the industrial CMP processing. The effect of chemical solution and the aqueous environment was observed to alter results for either prolonged exposure or lack of solution in the contact space. When patterned samples were exposed to KOH solutions for over 1 h, a low contact force (order of nanonewtons) AFM topography imaging was observed to deform and cause a material removal process on the surface with grooving on the order of 5–10 nm. This is believed to be due to a chemical softening of the materials, which leads to material removal even at low contact pressures. Though only an alkaline KOH environment was present and passivation of Cu is expected at neutral pH,[48] the formation of Cu hydroxides that are soluble in the alkaline KOH is possible.[49] The soluble $Cu(OH)_2$ may create a softened reactive layer that is easily removed. As seen in the results, overt etching of the copper films was not present in the exposure durations of our tests; thus, a near-surface effect may be present and affect the nanoscratch results to some degree. The COFs measured during nanoscratching (μ = 0.3–0.6) are similar to measurements with alumina and oxide slurries in contact with Cu.[48,50] It is estimated that the Cu reaction layer, when exposed to solutions for long durations, is on the order of 5 nm in thickness,[51] as was observed in pH 9 slurries in contact with Cu,[52] which is consistent with our result. Enhanced material removal during imaging was also observed for the carbon-doped oxide LK materials, which is expected at high pH. The removal was also observed with SEM, showing distinct wear grooves and material deformation on the surface in the AFM scanning directions. When diamond-coated AFM probes were used for AFM-based scratch tests in a dry environment, significant probe tip wear was observed. This was due to the lack of an aqueous environment lubricating the contact between the particle analog and the substrate at the applied scratch loads. The probe wear was detrimental to accurate contact analysis because the varying tip shapes and dimensions would alter

the contact conditions. Clearly, performing tests in an aqueous environment was important for adequate understanding of the lateral and normal deformations reported.

Conclusions

The creation of surface defects during CMP of Cu/LK patterned substrates was simulated by utilizing a diamond-coated AFM probe as an analog of a nanoscale individual abrasive particle. AFM force lithography was performed on various structures from a patterned wafer made with different porous LK dielectrics under a KOH environment. The effects of the lateral force on the structures were investigated in two categories: scratch depth of copper interconnects and lateral line pattern deformation.

The profiles of scratches on both materials showed that the deformation of the dielectric film was negligible compared to that of the copper interconnects. Both scratch depth and pileup increased as higher normal loads were applied. The copper film in the presence of the weaker, more porous LK dielectric film was far more susceptible to plastic deformation, and structure patterns with higher densities of copper showed an increase in normal surface deformation of the copper lines. COFs of the liquid-based nanoscratches had values of 0.3–0.6, measured using lateral force microscopy. Critical normal loads to initiate deformation were estimated and found to vary from 1.1 to 8.8 μN. A lateral deformation of the line patterns showed trends, indicating that the structures with a larger dielectric film width and with the stiffer dielectric material were more resistant to deformation, and the critical initiation loads ranged from 5.3 to 10.6 μN. From a sliding contact mechanics model, the experimental results correlated with the concept of an effective film modulus. Slopes of the deformation to load data compared well with the ratios of the effective modulus and the pattern densities and line widths. Copper deformation was shown to occur at lower loads in the model due to the high modulus-to-hardness ratio compared with the LK dielectrics tested. The integration of porosity to improve insulation weakened the oxide films and led to a decrease in the effective Cu/LK film modulus, resulting in an increased defect depth. Furthermore, the model showed that the Cu/LK interface was more sensitive to the change in dielectric film properties than the Cu normal deformation.

The results presented here give insight into the contact pressures and size effects necessary for defect formation, and indicate that at relatively low contact pressures, sufficient defect formation is observed, which follows suspected and observed results during polishing. AFM-based studies in liquid environments to simulate CMP conditions are a valid and useful tool to investigate the performance of advanced materials and pattern geometries. The techniques can be employed to drive the design of multilevel interconnects and integration of materials for substrates where CMP is performed and the issue of defectivity may be a concern. A priori understanding of electronic materials response to CMP conditions improves the efficiency of the design, manufacture, and integration time to bring materials to market.

Acknowledgments

The authors warmly thank the Intel Corporation for the financial support and for providing samples, and Dr. Paul Fischer and Professor Joseph A. Levert for helpful discussions.

State University of New York at Stony Brook assisted in meeting the publication costs of this article.

References

1. A. Brown, *IEEE Spectrum*, **42**, 40 (2005).
2. K. A. Perry, *Dig. Tech. Pap. - Symp. VLSI Technol.*, **1998**, 2.
3. M. McCoy, *Chem. Eng. News*, **83**, 20 (2005).
4. A. A. Volinsky, J. B. Vella, and W. W. Gerberich, *Thin Solid Films*, **429**, 201 (2003).
5. T. Hara, in *Proceedings of the 19th International VLSI Multilevel Interconnection Conference*, IMIC Publishers, p. 161 (2002).
6. S. Wang, G. Grover, C. Baker, J. Chamberlain, and C. Yu, *Solid State Technol.*, **44**, S9 (2001).
7. S. Kondo, S. Tokitoh, B. U. Yoon, A. Namiki, A. Sone, N. Ohashi, K. Misawa, S. Sone, H. J. Shin, T. Yoshie, et al., in *Proceedings of the International Interconnect Technology Conference (IITC)*, IEEE, pp. 86–88 (2003).
8. T. Scherban, B. Sun, J. Blaine, C. Block, B. Jin, and E. Andideh, in *Proceedings of the International Interconnect Technology Conference (IITC)*, IEEE, pp. 257–259 (2001).
9. P. Leduc, M. Savoye, S. Maitrejean, D. Scevola, V. Jousseaume, and G. Passemard, in *Proceedings of the International Interconnect Technology Conference (IITC)*, IEEE, pp. 209–211 (2005).
10. X. T. Chen, Y. T. Tan, Y. W. Chen, C. Y. Li, S. Balakumar, K. Chew, and P. D. Foo, in *Proceedings of the 19th International VLSI Multilevel Interconnection Conference*, IMIC Publishers, p. 156 (2002).
11. T. Hara, M. Uchica, M. Fuimoto, T. K. Doy, S. Balakumar, and N. Babu, *Electrochem. Solid-State Lett.*, **7**, G28 (2004).
12. A. K. Sikder, P. Zantye, S. Thagella, A. Kumar, B. M. Vinogradov, and N. V. Gitis, in *Proceedings of the Eighth International Chemical-Mechanical Planarization for ULSI Multilevel Interconnection Conference*, IMIC Publishers, p. 120 (2003).
13. N. Endo, S. Kondo, S. Tokitou, B. U. Yoon, N. Ohashi, S. Sone, H. J. Shin, I. Matsumoto, and N. Kobayashi, in *Proceedings of the Eighth International Chemical-Mechanical Planarization for ULSI Multilevel Interconnection Conference*, IMIC Publishers, p. 101 (2003).
14. K. Sikder, S. Thagella, A. Kumar, and J. Yota, *J. Mater. Res.*, **19**, 996 (2004).
15. E. Busch and S. Hosali, *Solid State Technol.*, **48**, 46 (2005).
16. S. Balakumar, X. T. Chen, Y. W. Chen, T. Selvaraj, B. F. Lin, R. Kumar, T. Hara, M. Fujimoto, and Y. Shimura, *Thin Solid Films*, **462–463**, 161 (2004).
17. P. Leduc, T. Farjot, M. Savoye, A.-C. Demas, S. Maitrejean, and G. Passemard, *Microelectron. Eng.*, **83**, 2072 (2006).
18. C. Yuan, W. D. van Driel, R. van Silfhout, O. van der Sluis, R. A. B. Engelen, L. J. Ernst, F. van Keulen, and G. Q. Zhang, *Microelectron. Reliab.*, **46**, 1679 (2006).
19. J. Vlassak, *J. Mech. Phys. Solids*, **52**, 847 (2004).
20. J. Bai, Y. W. Zhao, and Y. G. Wang, *Appl. Surf. Sci.*, **253**, 8489 (2007).
21. G. Fu, A. Chandra, S. Guha, and G. Subhash, *IEEE Trans. Semicond. Manuf.*, **14**, 406 (2001).
22. J. Luo and D. A. Dornfeld, *IEEE Trans. Semicond. Manuf.*, **14**, 112 (2001).
23. S. Thagella, A. K. Sikder, and A. Kumar, *J. Electrochem. Soc.*, **151**, G205 (2004).
24. K. Qin, B. Moudgil, and C.-W. Park, *Thin Solid Films*, **446**, 277 (2004).
25. W. Che, Y. Guo, A. Chandra, and A.-F. Bastawros, *J. Manuf. Sci. Eng.*, **127**, 545 (2005).
26. A. Chandra, P. Karra, A. F. Bastawros, R. Biswas, P. J. Sherman, S. Armini, and D. A. Luca, *CIRP Ann.*, **57**, 559 (2008).
27. W. A. Ducker, T. J. Senden, and R. M. Pashley, *Nature (London)*, **353**, 239 (1991).
28. X. Y. Lin, F. Creuzet, and H. Arribart, *J. Phys. Chem.*, **97**, 7272 (1993).
29. I. Sokolov, Q. K. Ong, H. Shodiev, N. Chechik, D. James, and M. Oliver, *J. Colloid Interface Sci.*, **300**, 475 (2006).
30. E. Taran, B. C. Donose, I. U. Vakarelski, and K. Higashitani, *J. Colloid Interface Sci.*, **297**, 199 (2006).
31. G. B. Basim, I. U. Vakarelski, and B. M. Moudgil, *J. Colloid Interface Sci.*, **263**, 506 (2003).
32. W. Che, Y. Guo, A. Chandra, and A. F. Bastawros, *J. Manuf. Sci. Eng.*, **125**, 731 (2003).
33. J. Ye, N. Kojima, K. Ueoka, J. Shimanuki, T. Nasuno, and S. Ogawa, *J. Appl. Phys.*, **95**, 3704 (2004).
34. F. Stevens, S. C. Langford, and J. T. Dickinson, *J. Appl. Phys.*, **99**, 023529 (2006).
35. D. Devecchio, P. Schmutz, and G. S. Frankel, *Electrochem. Solid-State Lett.*, **3**, 90 (2000).
36. N. Saka, T. Eusner, and J.-H. Chun. *CIRP Ann.*, **57**, 341 (2008).
37. J. L. Hutter and J. Bechhoefer, *Rev. Sci. Instrum.*, **64**, 1868 (1993).
38. R. W. Stark, T. Drobek, and W. M. Heckl, *Ultramicroscopy*, **86**, 207 (2001).
39. J. M. Neumeister and W. A. Ducker, *Rev. Sci. Instrum.*, **65**, 2527 (1994).
40. J. E. Sader, *Rev. Sci. Instrum.*, **66**, 4583 (1995).
41. G. M. Hamilton and L. E. Goodman, *J. Appl. Mech.*, **88**, 371 (1966).
42. G. M. Hamilton, *Proc. Inst. Mech. Eng., Part C: Mech. Eng. Sci.*, **197**, 53 (1983).
43. K. L. Johnson, *Contact Mechanics*, Cambridge University Press, New York (1987).
44. J. A. Williams, *Engineering Tribology*, Cambridge University Press, New York (2005).
45. D. Bozkaya and S. Müftü, Paper IJTC2008-71122 presented at the *Proceedings of the STLE/ASME International Joint Tribology Conference* (2008).
46. D. B. Bogy, *J. Appl. Mech.*, **35**, 460 (1968).
47. D. B. Bogy, *J. Appl. Mech.*, **38**, 377 (1971).
48. H. Liang, J.-M. Martin, and R. Lee, *J. Electron. Mater.*, **30**, 391 (2001).
49. S.-H. Chiu, Y.-L. Wang, C.-P. Liu, S.-C. Chang, G.-J. Hwang, M.-S. Feng, and C.-F. Chen, *Thin Solid Films*, **498**, 60 (2006).
50. G. Xu, H. Liang, J. Zhao, and Y. Li, *J. Electrochem. Soc.*, **151**, G688 (2004).
51. P. Bernard, S. Valette, S. Daveau, J. C. Abry, P. Tabary, and Ph. Kapsa, *Tribol. Int.*, **41**, 416 (2008).
52. T. Kanki, T. Shirasu, S. Takesako, M. Sakamoto, A. A. Asneil, N. Idani, T. Kimura, T. Nakamura, and M. Miyajima, in *Proceedings of the IEEE International Interconnect Technology Conference (IITC)*, IEEE, pp. 79–81 (2008).